Journal of the Optical Society of America B

OPTICAL PHYSICS

Optimizing performance for on-chip SBS-based isolator

CHOON KONG LAI,[1,2,*] MORITZ MERKLEIN,[1,2] ALVARO CASAS-BEDOYA,[1,2] YANG LIU,[3] STEPHEN J. MADDEN,[4] CHRISTOPHER G. POULTON,[5] MICHAEL J. STEEL,[6] AND BENJAMIN J. EGGLETON[1,2]

[1]The University of Sydney Nano Institute (Sydney Nano), The University of Sydney, Camperdown, NSW 2006, Australia
[2]Institute of Photonics and Optical Science (IPOS), School of Physics, The University of Sydney, Camperdown, NSW 2006, Australia
[3]Institute of Physics, Swiss Federal Institute of Technology Lausanne (EPFL), CH-1015, Lausanne, Switzerland
[4]Deparment of Quantum Science and Technology, Research School of Physics, Australian National University, Acton, Canberra, ACT 2601, Australia
[5]Institute School of Mathematical and Physical Sciences, University of Technology Sydney (UTS), Sydney, NSW 2007, Australia
[6]MQ Photonics Research Centre, School of Mathematical and Physical Sciences, Macquarie University, Sydney, NSW 2109, Australia
*Corresponding author: choon.lai@sydney.edu.au

Received 2 November 2022; revised 25 December 2022; accepted 12 January 2023; posted 13 January 2023; published 0 MONTH 0000

Non-reciprocal optical components such as isolators and circulators are crucial for preventing catastrophic back-reflection and controlling optical cross talk in photonic systems. While non-reciprocal devices based on Brillouin intermodal transitions have been experimentally demonstrated in chip-scale platforms, harnessing such interactions has required a suspended waveguide structure, which is challenging to fabricate and is potentially less robust than a non-suspended structure, thereby limiting the design flexibility. In this paper, we numerically investigate the performance of a Brillouin-based isolation scheme in which a dual-pump-driven optoacoustic interaction is used to excite confined acoustic waves in a traditional ridge waveguide. We find that acoustic confinement, and therefore the amount of Brillouin-driven mode conversion, can be enhanced by selecting an appropriate optical mode pair and waveguide geometry of two arsenic-based chalcogenide platforms. Further, we optimize the isolator design in its entirety, including the input couplers, mode filters, the Brillouin-active waveguide as well as the device fabrication tolerances. We predict such a device can achieve 30 dB isolation over a 38 nm bandwidth when 500 mW pump power is used; in the presence of a ±10 nm fabrication-induced width error, such isolation can be maintained over a 5–10 nm bandwidth.

https://doi.org/10.1364/JOSAB.479629

1. INTRODUCTION

Miniaturizing functionality that allows unidirectional transmission of optical signals is one of the key priorities in photonics research. This requires breaking Lorentz reciprocity [1] which has traditionally been achieved by Faraday rotation in magneto-optic garnets [2]. While on-chip integration is challenging because of apparent incompatibilities such as high lattice and thermal mismatch with common semiconductor substrates, there has been consistent progress in pursuing integrated magnetic isolators by means of hybrid bonding [3–7] or the direct-deposition method [8,9], with impressive results—3 dB insertion loss (IL) and 40 dB isolation ratio (IR)—in the latter case [9]. However, such an isolator relies on the non-reciprocal phase shift between the forward and backward propagation modes in a resonator, and therefore the operational bandwidth is very limited.

On the other hand, magnetic-free isolators can be realized by exploiting second-order [10] or third-order (Kerr) optical non-linearities [11–18]. These non-linear isolators rely on the injection of substantial power in the forward direction to prevent backward light propagation; as a result, they can only operate in a specific signal power range and are incapable of blocking a weak backward signal in the case of intense forward power [19]. Recent research has also focused on inducing spatiotemporal modulation of light in a non-magnetic optical waveguide [19–37]. This class of non-reciprocity relies on intermodal photonic transitions driven by electro-optic or acousto-optic effects. Excellent performance of acousto-optic non-reciprocity has been reported in aluminum nitride on silicon rib waveguides [34], with a <0.6 dB IL, ~ 16 dB IR, and >100 GHz operational bandwidth.

An alternative route to acousto-optic non-reciprocity is to use stimulated Brillouin scattering (SBS)—a phenomenon in which an optically driven acoustic wave promotes an optical modal transition with a typical frequency shift in the gigahertz (GHz) range. Such transitions can be either intramodal or intermodal and occur in the same or opposite propagation direction of the optical pump depending on the phase-matching condition of both optical modes involved. The four types of SBS are often referred to as backward SBS [38–44], backward intermodal SBS [45], forward SBS [46], and forward intermodal SBS (FIBS) [47]. Among them, FIBS was proposed in the earlier Brillouin isolation schemes in optical fibers [21] and planar waveguides [23] because of its large operational bandwidth arising from the almost parallel dispersion profile between the co-propagating fundamental and higher-order optical spatial modes, such that phase matching between them can be maintained over a large wavelength range. Later, isolators based on non-local interband Brillouin scattering (NIBS) were experimentally demonstrated in a suspended silicon structure [33]. Such NIBS process is generated by a pair of asymmetrical rib waveguides placed in close proximity, where FIBS is first excited by pumping one of the waveguides, and the mediating shear waves—known as Lamb waves [48]—travel to the adjacent waveguide through the silicon slab, allowing a similar optical intermodal transition to occur at the adjacent waveguide which carries the optical signal.

Suspended structures, however, are sophisticated waveguide structures requiring complex fabrication processes; furthermore, the integration of these waveguides in future multilayer structures may prove challenging. In addition, silicon suffers from non-linear losses and free-carrier absorption, which in turn limits the net Brillouin amplification [48,49]. It would be highly advantageous therefore to have an entirely embedded structure in which these non-reciprocal Brillouin effects may be harnessed in a material that lacks non-linear loss. However, such an embedded structure itself presents considerable design challenges.

Foremost, the performance of the isolator is highly dependent on the presence of shear waves in the waveguide. The effect of shear components was assumed to be negligible in earlier studies [23] but will affect both the acoustic confinement as well as the overall Brillouin gain. Rib waveguides, which are highly successful for backwards SBS in embedded structures, also support Lamb waves that can transport energy away from the core and are unsuitable for acoustic guidance in the forward direction. On the other hand, embedded waveguides also support a wide range of optical and acoustic modes, all of which will possess different coupling, losses, and Brillouin gain. In addition, a functional isolator must also include a mode coupler that can be integrated into the chip structure for exciting the desired optical spatial modes in the Brillouin active waveguide. The combination of waveguide and coupler design, together with fabrication constraints, together with the necessary conditions for an isolator to be useful, presents a challenging and complex design problem.

This article provides a detailed design strategy for realizing an isolation scheme based on FIBS in a non-suspended waveguide. We carry out a rigorous study of the complete device using established photonics simulation tools to examine the acoustic confinement and optimize the performance of each on-chip component involved. By performing full electromagnetic simulations of the couplers and combining this with accurate coupled-mode analysis of the SBS process in the Brillouin-active waveguide, we demonstrate that the acoustic guidance can be enhanced by selecting an appropriate combination of rectangular waveguide dimensions and pairs of optical spatial modes. We use our design strategy to optimize an isolator structure in an embedded chalcogenide ridge waveguide; we predict such a device can achieve 30 dB isolation over a 38 nm bandwidth for moderate pump powers (∼500 mW). Our strategy of mode selection also allows us control over the bandwidth of the device: we show that our design maintains isolation over a 5 nm (10 nm) bandwidth at −10 nm (+10 nm) fabrication-induced width error with a reasonable input optical power of 500 mW. The choice of a ±10 nm width deviation in our calculation is within the achievable precision of advanced fabrication tools such as electron beam lithography, dry-etching system, scanning electron microscope, etc., and thus it is a conservative guideline to follow in the future fabrication work. These structures therefore offer a viable alternative route to non-reciprocity, based on fully embedded waveguides.

The design concept of the whole device and its working principle is first described in the following section. Section 3 focuses on interrogating the key quantities (Brillouin shift, acoustic phase velocity v_p, and gain coefficient) for different spatial optical mode pairs at different waveguide dimensions of two different chalcogenide platforms (As_2S_3 and As_2Se_3). In Section 4 we show how the isolation bandwidth can be optimized by tailoring the waveguide dispersion. Further, we compute overall device performance after incorporating a broadband and dimensional tolerant mode coupler. Finally, a method for improving the device isolation is proposed in Section 5.

2. WORKING PRINCIPLE

The Brillouin-based non-reciprocal effect in this work relies on the FIBS process [50], which can be summarized by the processes in the schematic dispersion diagram in Fig. 1. The two pump channels ω_1 and ω_2 described in the figure may occupy either different spatial modes or polarization states [47]. Then the acoustic modes mediating the transition between the two optical modes of interest can be of different symmetry and character (quasi-flexural, quasi-torsional, and quasi-longitudinal modes) [51]. This work focuses on different optical spatial modes with the same polarization state because, as outlined in Section 3, inter-polarization Brillouin coupling is incapable of generating sufficiently large acoustic wavenumbers to fulfill the acoustic wave guiding requirements.

In the proposed isolation scheme, two co-propagating optical waves at angular frequencies ω_1 and ω_2 induce a coherent acoustic oscillation at frequency Ω and wavenumber q through electrostriction and radiation pressure. Pump ω_1 scatters off this dynamic grating and experiences a Brillouin shift to ω_2. The blue and red curves in Fig. 1 indicate slower and faster propagating optical modes. By phase-matching arguments, the frequency and wavenumbers of the three waves are related by $\Omega = \omega_1 - \omega_2$ and $q = k_1 - k_2$. For a specific waveguide structure, the Brillouin shift Ω at a particular acoustic wavenumber is determined by the acoustic dispersion curve (the green dashed curve). Meanwhile, a third co-propagating optical wave ω_3 with weak amplitude and small frequency separation from ω_1 can be scattered by the same acoustic wave and experience the same

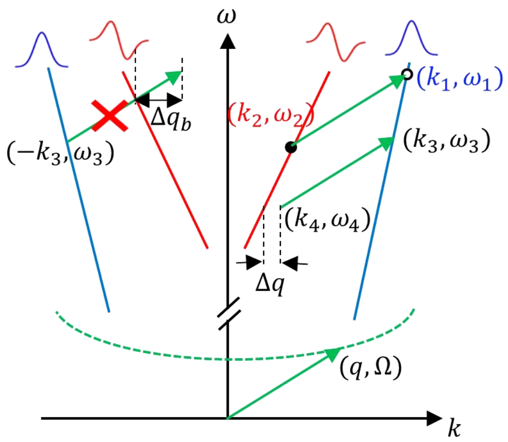

Fig. 1. Dispersion diagram describing the Brillouin-based non-reciprocal effect.

Brillouin shift to $\omega_4 = \omega_3 - \Omega$ provided the phase mismatch, $\Delta q = k(\omega_3) - k(\omega_4) - q$, is negligible. On the other hand, the corresponding scattering of a counter-propagating optical wave ω_3 is forbidden owing to a large phase mismatch ($\Delta q_b \gg \Delta q$).

The proposed design of the integrated isolator is depicted in Fig. 2(a). The whole device comprises a pair of reciprocal mode couplers MC1 and MC2, a multimode waveguide [the non-reciprocal mode coupler (NRMC)], and several mode-size converters linking different optical components. Two continuous pump waves of frequency ω_1 and ω_2 are launched into Port 1 and Port 3, respectively. Ideally, light entering all ports propagates in the fundamental optical spatial mode in the waveguide. After propagating through the first mode multiplexer MC1, the mode nature of pump ω_1 remains unchanged while pump ω_2 undergoes mode conversion to a higher-order mode via linear coupling. The intensity beat note of pumps ω_1 and ω_2 induces an acoustic wave that enables coherent forward scattering, whereby a co-propagating signal wave ω_3 injected from Port 1 is converted to a higher-order optical mode at ω_4, which is then demultiplexed at the second mode coupler MC2 and output at Port 4. The output power from Port 2 is negligible if the mode conversion efficiency from both the FIBS process and mode demultiplexing at MC2 approaches 100%. On the other hand a signal wave at ω_3 input from Port 2 will be transmitted to Port 1 without experiencing any FIBS-induced mode conversion.

It has been shown previously [23] that a better non-reciprocal mode conversion efficiency can be achieved by increasing the initial power ratio of the forward pump ω_1 to that of the pump ω_2 such that the power of the forward acoustic wave peaks at the middle of the NRMC [23]. The plot in Fig. 2(a) illustrates a typical power variation of the pump and signal waves along the NRMC with an initial pump power ratio of ∼0.99. The waveguide width variation in the proposed design is clearly illustrated in Fig. 2(b). Ports 1, 2, 3, and 4 have a horizontal width w (∼1.9 µm) that is mode-match to a lens-tipped fiber with Gaussian spot size of ∼2 µm and minimizes sidewall scattering loss that is particularly relevant when a long integrated circuit is required for future applications. Therefore, two different spot size converters (SSCs) are used to narrow down the horizontal width w of Port 1 and Port 3 into the required dimensions of the parallel waveguides in MC1, and a horizontal taper is used to further shrink the waveguide into the width required by the NRMC. Likewise, another half of the device requires similar horizontal tapers and SSCs to expand the waveguide into the width of Ports 3 and 4.

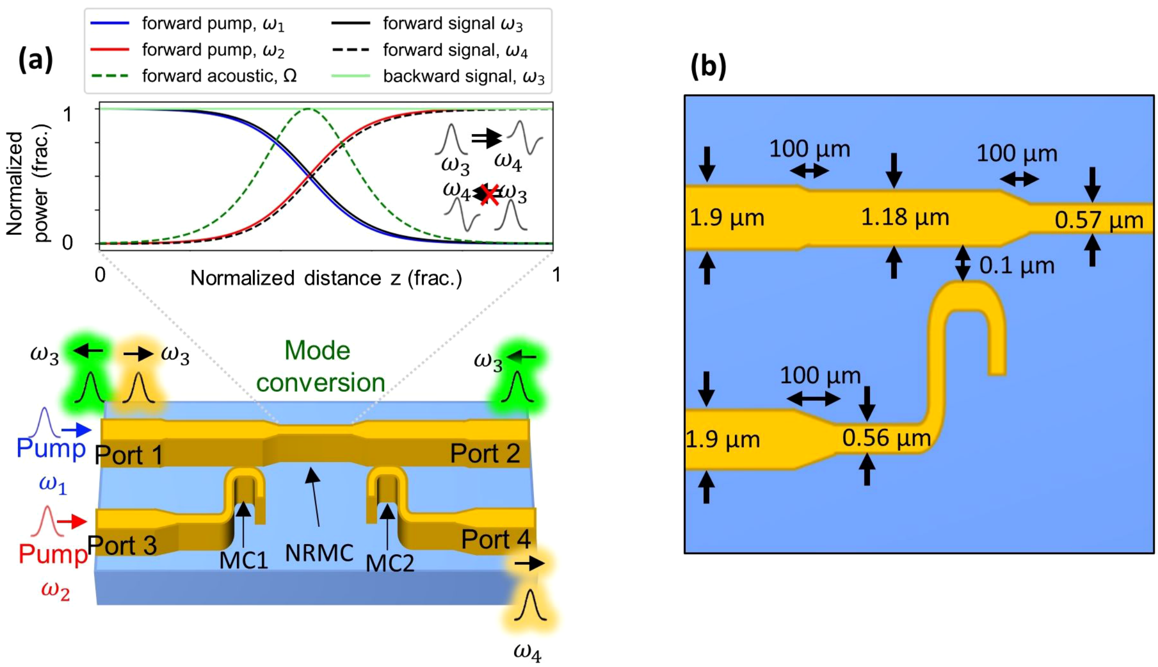

Fig. 2. (a) Schematic of the Brillouin-based optical isolator. The plot in the figure illustrates the normalized power of all optical and acoustic waves traveling at each position of the non-reciprocal mode coupler NRMC. (b) Top view showing the waveguide width variation in the first half of the proposed isolator device.

3. OPTICAL AND ACOUSTIC CONFINEMENT IN A NON-SUSPENDED CHALCOGENIDE WAVEGUIDE

The primary challenge of the proposed Brillouin isolation scheme is to achieve strong optical and acoustic guidance for co-propagating waves in a non-suspended waveguide. For both optical and acoustic waves, this can be realized by ensuring that the mode has a lower phase velocity in the waveguide core than that of all propagating modes in the cladding. Various chalcogenide platforms such as GeSbS [52] and As_2S_3 [38–44] can achieve this in backward SBS process as they exhibit a lower phase speed of both light and sound compared with silica, which can be used as a cladding material. However, as illustrated in Fig. 1, the phase-matching condition in the forward SBS process results in a much smaller q (longer elastic wavelengths) as compared with the backward counterparts. Such long elastic wavelengths involved in the FIBS process pose a major challenge: these wavelengths are very close to or even beyond the elastic mode cut-off regime, making acoustic confinement more difficult.

Our numerical modeling of acoustic modes suggests that standard shallow-etched As_2S_3 rib waveguides do not possess appropriate acoustic guided modes for FIBS. However, such guided modes can be found with a further increase in the etch depth or using a fully etched (strip) waveguide. Such improvement in the acoustic guidance is achieved by increasing the acoustic wavenumber q, which is determined by the effective index difference between the two optical spatial modes of interest if the optical wavelength is fixed. This also suggests that, apart from the waveguide dimensions and choices of optical mode pairs, selecting a higher refractive index material with similar acoustic properties could further improve the acoustic confinement.

To investigate the impact of the geometric parameters on the acoustic confinement, we solve the elastic and optical mode problems and find the Brillouin gain coefficients for waveguides of several different dimensions of silica-clad arsenic sulfide (As_2S_3) and a higher-index arsenic selenide (As_2Se_3) multimode waveguides using the open-source Numerical Brillouin analysis tool (NumBAT) [61,62], which has been validated against a number of reported experimental results [63–66]. Arsenic trisulfide (As_2S_3) is a mature on-chip SBS platform that has been substantially studied for a decade [38–44]. While on-chip SBS has not yet been demonstrated in the selenide platform (As_2Se_3), a high SBS gain has been observed in selenide fibers [54]. Together with its high refractive index, excellent acoustic guidance is anticipated in the same waveguide dimension.

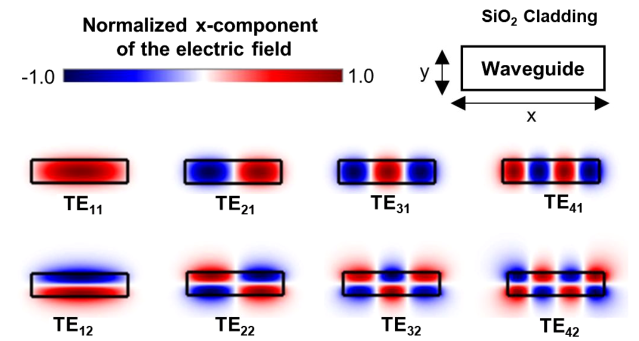

Fig. 3. Normalized electric field distribution of different quasi-transverse electric (TE) spatial modes in a rectangular waveguide. They are labeled in a conventional way as TE_{pq} where p and q indicate the number of horizontal and vertical lobes, respectively.

The relevant physical properties of As_2S_3 and As_2Se_3 are shown in Table 1. From the stiffness tensor components c_{ij}, the longitudinal (v_l) and shear speeds of sound (v_s) in each material can be computed using the relations

$$v_l = \sqrt{\frac{c_{11}}{\rho}}, \quad v_s = \sqrt{\frac{c_{44}}{\rho}}. \tag{1}$$

A parametric sweep of waveguide dimensions was executed to study the strength of acoustic guidance. For silica-clad sulfide (As_2S_3) waveguides, a width w scan from 600 to 3000 nm was performed at three different vertical thicknesses of 500, 700, and 1000 nm. To investigate the effect of refractive index on the acoustic confinement, we performed a similar width scan on a higher-index selenide (As_2Se_3) waveguide with 700 nm vertical thickness. Furthermore, while it is likely more feasible to induce FIBS with the two lowest-order modes TE_{11} and TE_{21}, the elastic mode confinement arising from other higher-order spatial modes listed in Fig. 3 is also computed to identify the best possible confinement and gain for each geometry.

In general, the degree of optical confinement can be described by the normalized propagation constant β, which is given by

$$\beta = \frac{n_{\mathrm{eff}} - n_{\mathrm{cl}}}{n_{\mathrm{co}} - n_{\mathrm{cl}}} = \frac{v_{\mathrm{co}}}{v_{\mathrm{eff}}}\left(\frac{v_{\mathrm{cl}} - v_{\mathrm{eff}}}{v_{\mathrm{cl}} - v_{\mathrm{co}}}\right), \tag{2}$$

where it can be expressed in terms of refractive indices or phase velocity. n_{eff}, n_{co}, and n_{cl} are effective mode index, core, and cladding refractive index. The corresponding phase velocities v_{eff}, v_{co}, and v_{cl} can be determined by the refractive index relation $n = c/v$ where c is the speed of light in vacuum. β is a good indicator of the optical confinement and has a value ranging

Table 1. Optical and Elastic Properties of As_2S_3, As_2Se_3, and SiO_2 Used in the NumBAT Simulation where n and ρ are Refractive Index at 1.55 μm Wavelength and Material Density, Respectively[a]

Material	n at 1.55 μm	ρ (kgm^{-3})	c_{11} (GPa)	c_{12} (GPa)	c_{44} (GPa)	p_{11}	p_{12}	p_{44}	η_{11}	η_{12}	η_{44}
SiO_2 [53–56]	1.45	2200	78.6	16.1	31.2	0.12	0.27	−0.075	1.6[b]	1.29[b]	0.16[b]
As_2S_3 [56–58]	2.44	3150	19.75	8.7	5.52	0.25	0.23	0.01	1.8[b]	1.45[b]	0.18[b]
As_2Se_3 [50,52,55,56]	2.84	4635	23.5	9.5	7.0	0.31	0.27	0.02	0.78[b]	0.63[b]	0.08[b]

[a] c_{ij}, p_{ij}, and η_{ij} are fourth rank stiffness, photoelastic, and phonon viscosity tensors in units of mPa.s expressed in the Voigt compact notation [53].
[b] is the theoretical estimate using the Smith *et al*. approach [56].

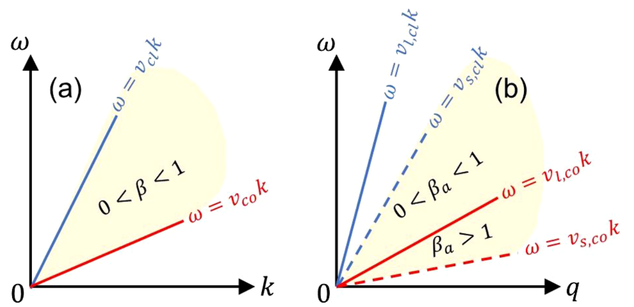

Fig. 4. (a) Optical and (b) acoustic dispersion plot showing the light and sound lines for the core and cladding material. The yellow region indicates the area where a confined mode can be found.

from 0 to 1. For instance, $\beta = 1$ means the optical field completely confined in the waveguide core while $\beta = 0$ represents zero confinement.

Likewise, a normalized propagation constant can be used to describe the acoustic confinement. The concept of using normalized propagation constant as a confinement metric for both optical and acoustic modes is depicted in Figs. 4(a) and 4(b). In comparison, the elastic wave propagation is rather complicated due to the existence of both transverse (shear) and longitudinal (compressive) mechanical field nature that give rise to different sound velocity in bulk materials. Therefore, instead of one light line for each material in the optical dispersion [Fig. 4(a)], two sound lines corresponding to the shear and longitudinal wave nature are drawn on the acoustic dispersion plot [see Fig. 4(b)]. For an embedded rectangular waveguide, a confined acoustic mode requires an effective phase velocity v_p smaller than the cladding shear speed $v_{s,\mathrm{cl}}$ while any numerical solutions with $v_p > v_{s,\mathrm{cl}}$ are considered as a free mode [67], in which energy is no longer being confined in the core; the confinement increases as v_p decreases from the cladding shear line. To facilitate the following discussion, we define the normalized acoustic propagation constant β_a as

$$\beta_a = \frac{v_{l,\mathrm{co}}}{v_p}\left(\frac{v_{s,\mathrm{cl}} - v_p}{v_{s,\mathrm{cl}} - v_{l,\mathrm{co}}}\right), \tag{3}$$

where $v_{l,\mathrm{co}}$ represents the core longitudinal speed. It is noteworthy that while the acoustic guidance is analogous to that of the optical counterpart, $\beta_a > 1$ is possible due to the existence of shear waves that propagate at a slower speed than the longitudinal (compressive) waves in the core ($v_{s,\mathrm{co}} < v_{l,\mathrm{co}}$), resulting in $v_p < v_{l,\mathrm{co}}$.

In Figs. 5(a)–5(d), we plot the normalized propagation constant β versus w for different waveguide structures and optical spatial modes at an optical pump wavelength of 1550 nm. In Figs. 5(e)–5(h) we investigate the behavior of different acoustic modes as a function of waveguide width w. We found that all numerical solutions within the parameter sweep range in Fig. 5 have $\beta_a < 1$. At a specific dimension and optical mode pair, there exists more than one solution that lies in the confinement window, from which we only select the mode that records the highest Brillouin gain coefficient g_0 to plot in Figs. 5(e)–5(h). The strength of the Brillouin coupling g_0 for each of these modes is computed through standard expressions based on optoacoustic mode overlap integrals [61,62].

From the optical dispersion diagram in Figs. 5(a)–5(d), one can see that the confinement for each TE_{pq} mode improves with the waveguide size. Further, the number of guided TE_{pq} modes—with normalized propagation constant above the so-called "cladding light line" ($\beta > 0$)—increases when w expands from 600 to 3000 nm, leading to a higher number of mode combination choices at a larger w. However, the trend of acoustic confinement in Figs. 5(e)–5(h) can be quite different from that of the optical counterpart. This is because, apart from waveguide dimension, β_a is also dependent on the normalized propagation constant difference between two optical modes of interest $\Delta\beta$, due to the fact that $q = k_1 - k_2$, as described in Fig. 1. For instance, for 500 nm thick As_2S_3 waveguides [Fig. 5(e)], the abrupt increase of β_a corresponding to $\mathrm{TE}_{11}-\mathrm{TE}_{12}$ pair (solid circle) at $w < 1200$ nm is likely due to the high $\Delta\beta$ between the TE_{11} and TE_{12} modes in Fig. 5(a). For $w > 1200$ nm, since there is no further increase in $\Delta\beta$, hence the increase of β_a in this width regime is solely caused by the increase of waveguide size. This relation between $\Delta\beta$ and β_a is also true for all other mode combinations and it explains why there is actually a decrease of β_a for $\mathrm{TE}_{11}-\mathrm{TE}_{21}$ (solid inverted triangle), $\mathrm{TE}_{11}-\mathrm{TE}_{22}$ (solid triangle), and $\mathrm{TE}_{41}-\mathrm{TE}_{42}$ (solid hexagon) pairs for a given w range in Fig. 5(h). While it can be deduced from plots (e)–(h) that the highest possible β_a among the available mode pairs increase with w, the impact of vertical thickness on the maximum β_a is not obvious from plots (e)–(g).

From Figs. 5(d) and 5(h) we see that switching to a higher-index selenide platform (As_2Se_3) can significantly improve the acoustic confinement, from $\beta_a \approx 0.3$ to $\beta_a \approx 0.7$ [compare plot (f) with (h)]. This is aligned with the previous observation that higher refractive index results in a higher q or $\Delta\beta$, and so should increase the acoustic confinement. Together with a larger photo-elastic coefficient, the Brillouin gain coefficient in the selenide (As_2Se_3) waveguide is approximately a factor of 3 over the sulfide (As_2S_3) platform. Despite the fact that such high theoretical gains can only be achieved if the processed waveguides are free from sidewall roughness-induced losses, the material's intrinsic optical and acoustic absorption and other detrimental factors, the gain improvement by a factor of 3 from the sulfide to selenide platforms is still promising provided their optical and acoustic losses are comparable.

By comparing Figs. 5(e)–5(h), it can be seen that the acoustic mode from the $\mathrm{TE}_{12}-\mathrm{TE}_{13}$ transition (solid square) exhibits excellent acoustic confinement in both material systems, with $\beta_a \approx 0.7$ in the selenide platform [see Figs. 6(i)–6(l)]. However, it is advantageous to use the lowest-order mode pairs possible because the higher-order counterparts often experience a greater fabrication-induced sidewall scattering loss and cross talk and can be difficult to couple into. The acoustic confinements for different dimensions for both lowest-order pairs $\mathrm{TE}_{11}-\mathrm{TE}_{21}$ (solid inverted triangle) and $\mathrm{TE}_{11}-\mathrm{TE}_{12}$ (solid circle) are shown in Fig. 5. We see that for the $\mathrm{TE}_{11}-\mathrm{TE}_{21}$ pair (solid inverted triangle), higher β_a is observed at a higher aspect ratio waveguide (small w and large t). On the other hand, it is preferable to have a lower aspect ratio waveguide for the $\mathrm{TE}_{11}-\mathrm{TE}_{12}$ pair (solid circle).

While all acoustic modes presented in Fig. 5 have $\beta_a < 1$, the displacement field u profile in Fig. 6 illustrates that they have strong shear (transverse) field components. The polarization

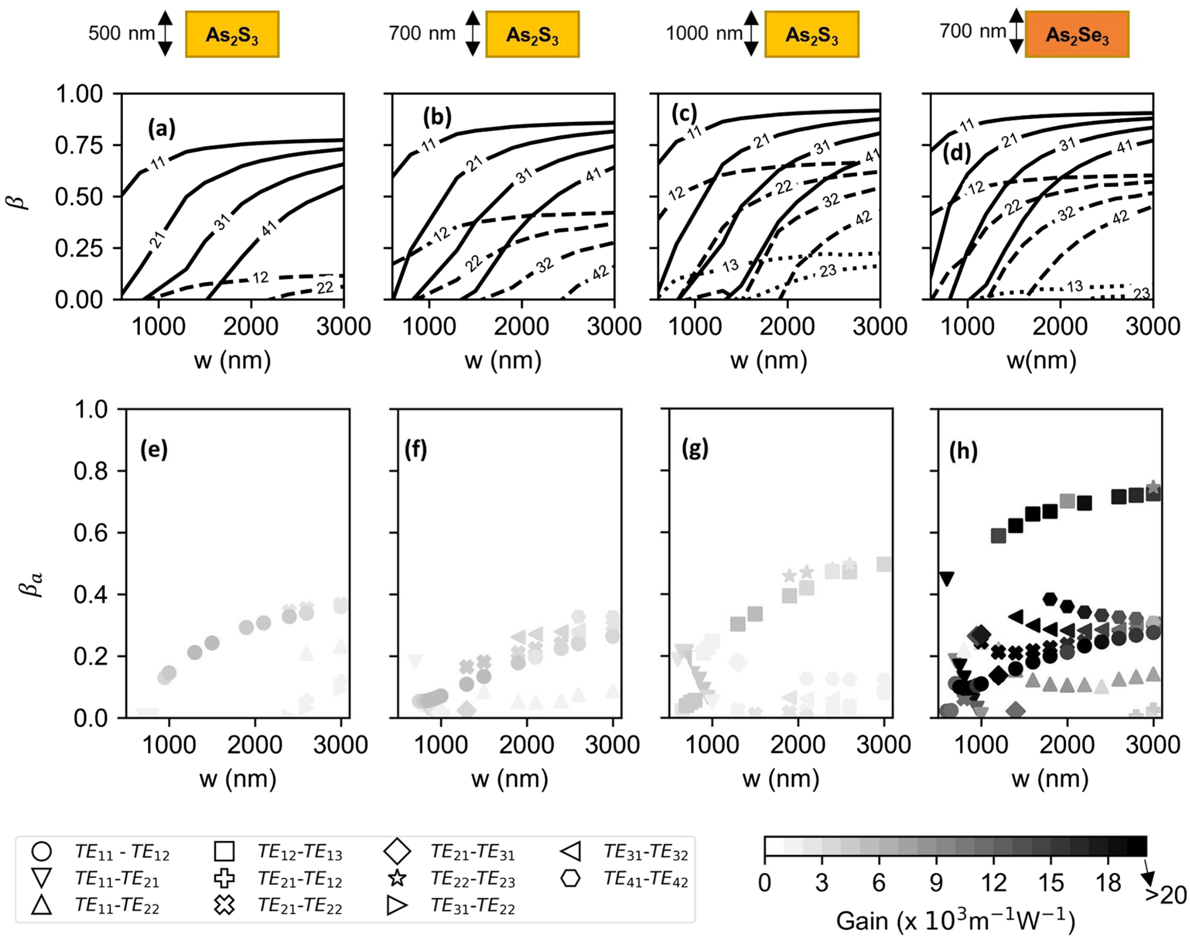

Fig. 5. Optical and acoustic confinement of As_2S_3 and As_2Se_3 waveguides: (a)–(d) optical dispersion diagram showing β variation with respect to the width w of As_2S_3 waveguides at a vertical thickness of (a) 500 nm, (b) 700 nm, and (c) 1000 nm; and (d) As_2Se_3 waveguides at 700 nm thickness for different quasi-transverse electric spatial modes TE_{pq} where the mode label pq is indicated by the inline label. Solid, dashed, and dotted lines are used to indicate $q = 1$, $q = 2$, and $q = 3$, respectively. (e)–(h) Plots of β_a of the guided acoustic modes versus w corresponding to the waveguide structures of (a)–(d), respectively. The shape of the scatter points represents different optical mode pairs in the bottom legend while the sequential color scales indicate the gain coefficient in units of m^{-1} W^{-1} according to the color bar.

of the transverse displacement field is dependent on the types of optical mode transition. In general, $TE_{pq}-TE_{(p+1)q}$ transition can induce a forward propagating acoustic wave with a strong lateral component of $\boldsymbol{u}_x$ [see Figs. 6(a)–6(d)], whereas the acoustic wave from $TE_{pq}-TE_{p(q+1)}$ transition has a strong $\boldsymbol{u}_y$ component [see Figs. 6(e)–6(h) and 6(i)–6(l)].

Altering the waveguide dimension can significantly change the confinement factor of such $\boldsymbol{x}$- and $\boldsymbol{y}$-polarized acoustic modes. Focusing on Figs. 5(g) and 5(h), the $\boldsymbol{x}$-polarized acoustic mode due to the $TE_{11}-TE_{21}$ transition loses its confinement when the horizontal width increases. Meanwhile, to suppress the $\boldsymbol{y}$-polarized acoustic mode due to the $TE_{11}-TE_{12}$ transition, one can increase the vertical thickness [see Figs. 5(e)–5(g)]. It is also worth mentioning that while the confinement of both acoustic modes can be improved by reducing the width and the thickness, further dimensional shrinkage ($w < 500$ nm and $t < 500$ nm) can lead to a converse effect as the optical modes can no longer be confined in such a small waveguide core.

4. OVERALL PERFORMANCE OF THE PROPOSED ISOLATOR

In the previous section, we have identified the optical mode pairs and waveguide dimensions of two binary chalcogenide platforms in which confined acoustic modes can be excited to yield high Brillouin gain. Next, we selectively study the narrow selenide (As_2Se_3) waveguide structures ($w < 600$ nm) based on the $TE_{11}-TE_{21}$ mode pair. This pair has been chosen because the resulting combination exhibits appreciable acoustic confinement ($\beta_a \approx 0.45$) and an excellent gain coefficient ($g_0 \approx 2.4 \times 10^4$ m^{-1} W^{-1}). We compute the overall isolator performance—isolation bandwidth—of such narrow selenide waveguide by solving the coupled-mode equations and also taking into account the mode coupler device performance.

A. Solving Coupled-Mode Equations

An isolator should operate over as broad a bandwidth as is feasible. For Brillouin-type isolators as considered here, detuning of the signals from the pumps gradually increases the phase

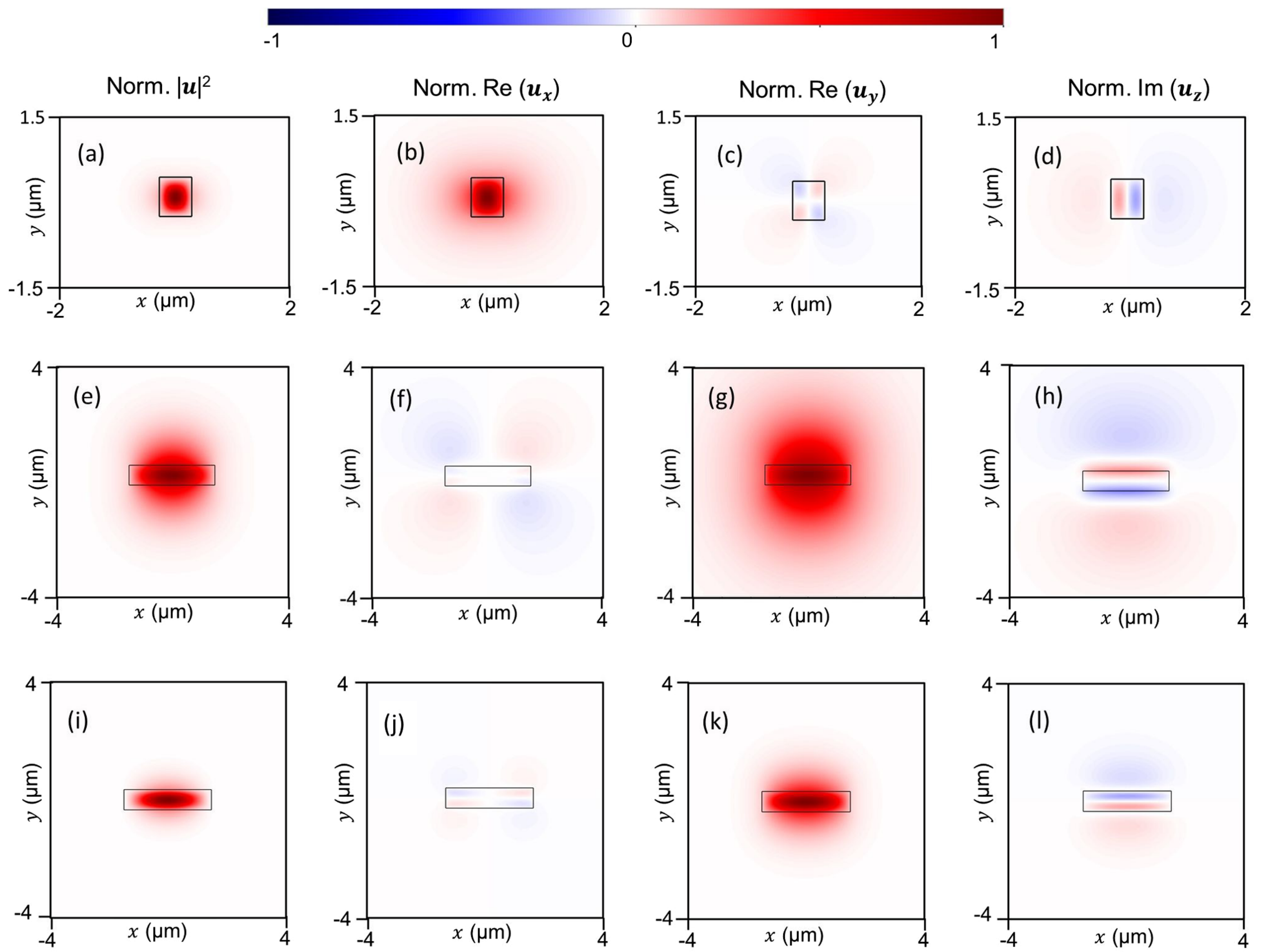

Fig. 6. Displacement field, $\boldsymbol{u}$ profile in the $\boldsymbol{x}-\boldsymbol{y}$ plane of 700 nm thick As_2Se_3 waveguide with (a)–(d) $TE_{11}-TE_{21}$ pair at $\boldsymbol{w}=570$ nm, (e)–(h) $TE_{11}-TE_{12}$ pair at $\boldsymbol{w}=3000$ nm, and (i)–(l) $TE_{12}-TE_{13}$ pair at $\boldsymbol{w}=3000$ nm. The first column (a), (e), (i) shows the square of the magnitude of the complex amplitude $|\boldsymbol{u}|^2$, followed by the real part of its $\boldsymbol{x}$ component (b), (f), (j), the real part of its $\boldsymbol{y}$ component (c), (g), (k), and the imaginary part of its $\boldsymbol{z}$ component (d), (h), (l).

mismatch between the acoustic and optical fields Δq, resulting in reduced mode conversion when the phase mismatch becomes too large. Here we investigate this effect quantitatively, with the aim of determining the bandwidth of our entire device.

For FIBS mode conversion, the change in field amplitudes with respect to the propagation distance, z of the two forward traveling pump waves (ω_1 and ω_2), and the two signal waves (ω_3 and ω_4) at a particular Δq are described by the equations [23,61]

$$\frac{\partial a_1}{\partial z}+\frac{\alpha_1}{2}a_1=-\frac{g_0}{2}|a_2|^2 a_1\,, \tag{4}$$

$$\frac{\partial a_2}{\partial z}+\frac{\alpha_2}{2}a_2=\frac{g_0}{2}|a_1|^2 a_2\,, \tag{5}$$

$$\frac{\partial a_3}{\partial z}+\frac{\alpha_3}{2}a_3=-\frac{g_0}{2}a_1^* a_2 e^{i\Delta q z}a_4, \tag{6}$$

$$\frac{\partial a_4}{\partial z}+\frac{\alpha_4}{2}a_4=\frac{g_0}{2}a_1^* a_2 e^{-i\Delta q z}a_3, \tag{7}$$

where $|a_i(z)|^2$ represents the physical power $P_i(z)$ in Watts carried in the optical fields, α_i is the optical propagation loss in m^{-1}, and g_0 is the Brillouin gain coefficient in $m^{-1}\ W^{-1}$. A full derivation is provided in Sections 3 and 4 of Supplement 1. Here Eqs. (4)–(7) describe the power flow from P_1 to P_2 and P_3 to P_4 along the waveguide, as shown in Fig. 1. It is important to note that, in Eqs. (4)–(7), the two strong "pumps" at $\omega_{1,2}$ generate an acoustic wave that drives transition between two "signals" at $\omega_{3,4}$. Here the pumps are assumed to have zero detuning but there is a phase mismatch of Δq between the signals. Also, the signal fields are assumed to be very weak in comparison with the pumps such that they do not affect the acoustic dynamics generated by the pumps. In previous work [23], it has been shown that the coupling efficiency can be maximized by increasing the ratio of input pump power $P_1(0)$ to $P_2(0)$. This is because the strength of the acoustic field slowly develops and reaches its maximum, instead of decreasing rapidly from $z=0$ as occurs for balanced pump powers. For the following study, the initial pump powers are fixed at $P_1(0)=0.999\ P_T$ and $P_2(0)=0.001\ P_T$ where P_T represents the total input pump power, which

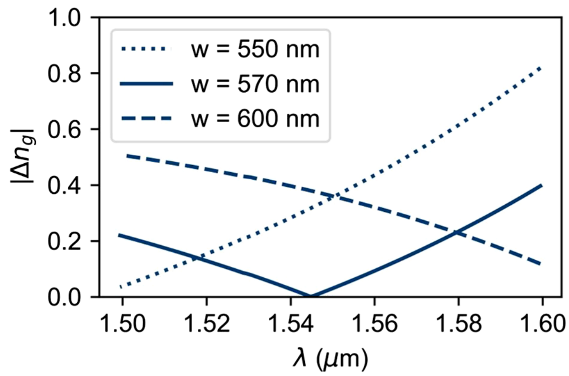

Fig. 7. Group index difference between TE_{11} and TE_{21} mode, $|\Delta n_g|$ versus λ at $w = 550, 570$, and 600 nm.

unless otherwise stated is taken to be $P_T = 500$ mW. The maximum isolation in decibels, I_{dB}, is defined as

$$I_{dB} = 10\log_{10}\left(\frac{P_3(z = L)}{P_3(z = 0)}\right), \quad (8)$$

where L is the waveguide length, and P_3 is the physical power of the signal at ω_3, with the initial signal power $P_3(0)$ fixed at 1 mW. Equations (4)–(7) can be solved numerically to obtain $P_i(z)$. It is important to note that while the device insertion loss increases with the optical loss α_i, the maximum isolation I_{dB} is independent on α_i because the power flow in both directions experiences the same propagation loss. Hence, $\alpha_i = 0$ is used in our calculation.

B. Isolation Bandwidth and Dispersion Engineering

The key to expanding the operational bandwidth is maintaining $\Delta q \approx 0$ for a wide range of detuning. The bandwidth $|\delta\omega|$ for which the FIBS can occur is then given by

$$|\delta\omega| = \frac{\pi}{2z_{max}}\frac{c}{\Delta n_g}, \quad (9)$$

where c is the speed of light in free space and Δn_g is the group index difference between the TE_{11} and TE_{21} modes at ω_1. In this equation, $\Delta n_g = n_{g,1} - n_{g,2}$ is the difference in optical group index, where the group index of mode i is given by $n_{g,i} \equiv c/(\frac{d\omega_i}{dk}) = n_i + \omega\frac{dn_i}{d\omega}$, where $n_i(\omega) = ck_i/\omega$ is the effective index of mode i. The analytical derivation of $|\delta\omega|$ in Eq. (9) can be found in Section 5 of Supplement 1. One way in which the operational bandwidth can be widened is by tailoring the waveguide dispersion (reducing Δn_g) by changing the waveguide dimensions (w or t). The effect of such tuning is shown in Fig. 7. Examining the $|\Delta n_g|$ across a 100 nm wavelength span for three different w (550, 570, and 600 nm), we find that waveguides of width $w = 570$ nm yield $|\Delta n_g| < 0.1$ for a 30 nm span around a central wavelength of 1550 nm, with a minimum $|\Delta n_g| \approx 7 \times 10^{-4}$ at $\lambda = 1544$ nm. It is important to note that, when computing the n_g, the refractive index of As_2Se_3 is fixed at 2.84 due to the flat response of material dispersion in the 1500–1600 nm wavelength range (see Section 7 of Supplement 1).

C. High-Performance Fabrication-Tolerant Mode Coupler

The overall performance of the isolator is inseparable from the quality of the mode filters [Fig. 2(a)]. Therefore, in addition to optimizing the FIBS process in the Brillouin-active region, it is also necessary to have a mode filter with high efficiency and low cross talk so that the isolation and the operational bandwidth of the whole device are as close as possible to the ideal bandwidth computed from Eqs. (4)–(7). In general, mode (de)multiplexing can be achieved using Y junctions [68], asymmetrical directional couplers (ADCs) [69,70], and multimode interference (MMI) couplers [71]. However, there is a strong motivation to use ADCs because (1) the methodology for improving the ADCs' dimensional tolerance has been well developed [69,70]; (2) the sharp corners of Y junctions often lead to fabrication challenges; and (3) MMI couplers experience higher radiation loss.

Here, we design a width-tolerant mode coupler for converting between TE_{11} and TE_{21} modes on the As_2Se_3 platform. We employ the strategy reported in [69]: ADCs are made of a pair of parallel waveguides with different widths w_1 and w_2, separated by a gap w_g as shown in Fig. 8(a). The supermode analysis and optimization process for such a ADC-based mode coupler is detailed in Section 6 of Supplement 1. The optimized dimension of the mode coupler has already been shown in Fig. 2(b), in which $w_1 = 562$ nm, $w_2 = 1185$ nm, $w_g = 100$ nm. The mode coupler has a coupling length $L_c = 12$ μm.

The simulated transmission spectrum of such an optimized design, subjected to a perturbation Δw, is plotted in Figs. 8(b)–8(e). From the results plotted in Fig. 8(e), a notably flat transmission response is obtained at the FIBS waveguide, with $f_{TE11}^{Back} \approx 1$, suggesting that the device insertion loss due to mode coupler cross talk is negligible. However, imperfect mode coupling ($f_{TE21}^{Port2} > 0$) can occur at any wavelength other than the optimum wavelength or when there is a small Δw [see Fig. 8(d)]. As a consequence, part of the light from the TE_{21} mode at ω_4 can output to Port 2 [see Fig. 2(a)], thus reducing the isolation bandwidth estimated from Eqs. (4)–(9).

D. Computation of Overall Performance

Based on the mode coupler performance in the previous section, the overall isolation, I'_{dB}, as a function of P_{total} and λ is then given by

$$I'_{dB}(P_{total}, \lambda) = 10\log_{10}\left(\frac{P_3(z = L)}{P_3(z = 0)} + f_{TE21}^{Port2}\right), \quad (10)$$

where $\frac{P_3(z=L)}{P_3(z=0)}$ is the linear power fraction of the non-converted TE_{11} mode from the FIBS process that output to Port 2 at ω_3 and f_{TE21}^{Port2} is the linear power fraction of the TE_{21} mode output to Port 2 at ω_4 due to imperfect mode coupling at the mode filter demonstrated in Section 4.C.

We further calculate the isolation bandwidth of the 570 nm × 700 nm As_2Se_3 waveguide using Eq. (10). A two-dimensional parameter sweep of P_T from 0.1 to 1 W and signal wavelength, $\lambda_s = 2\pi c/\omega_3$ from 1500 to 1600 nm was performed for a waveguide length $L = 2$ cm. Such a length is sufficient to achieve complete mode conversion for a reasonable

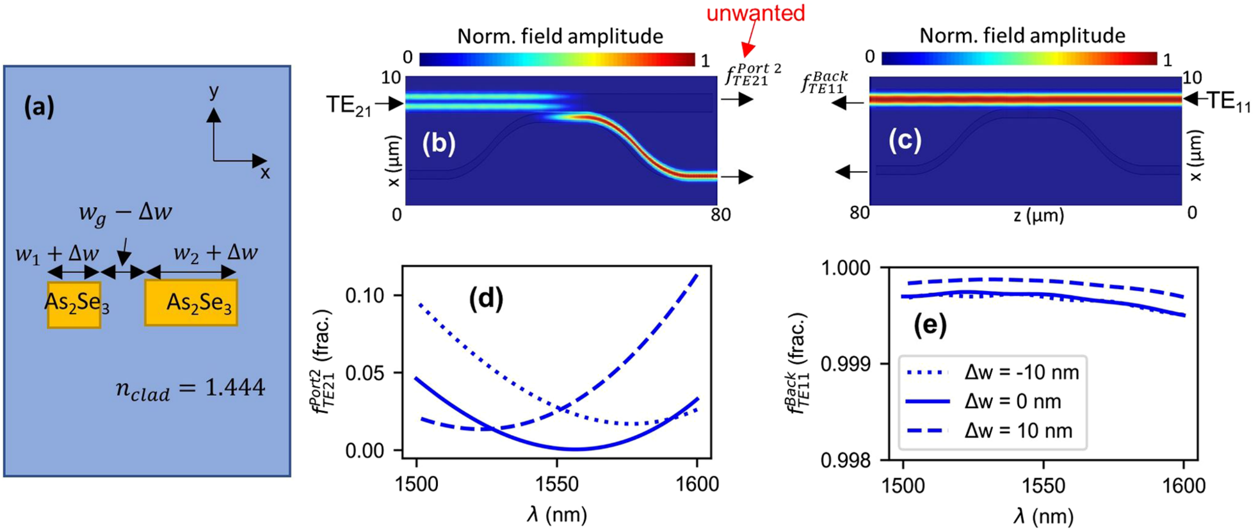

Fig. 8. (a) The image depicts the cross section of a pair of parallel waveguides with widths w_1 and w_2 separated by a gap, w_g; (b)–(e) Lumerical 3D FDTD simulation for mode coupler with $w_1 = 562$ nm, $w_2 = 1185$ nm, $w_g = 100$ nm, $L_c = 12$ μm: (b)–(d) TE_{21} mode injection from FIBS waveguide and output at Port 2 and Port 4 as TE_{21} and TE_{11} modes, with its (b) top view of the field propagation, and (d) the plot of f_{TE21}^{Port2} versus λ for different Δw; (c)–(e) TE_{11} mode injection from Port 2 and output at FIBS waveguide, with its (c) top view of the field propagation, the spectrum of (e) f_{TE11}^{Back} for $\Delta w = -10$ nm, 0 nm, and 10 nm, respectively.

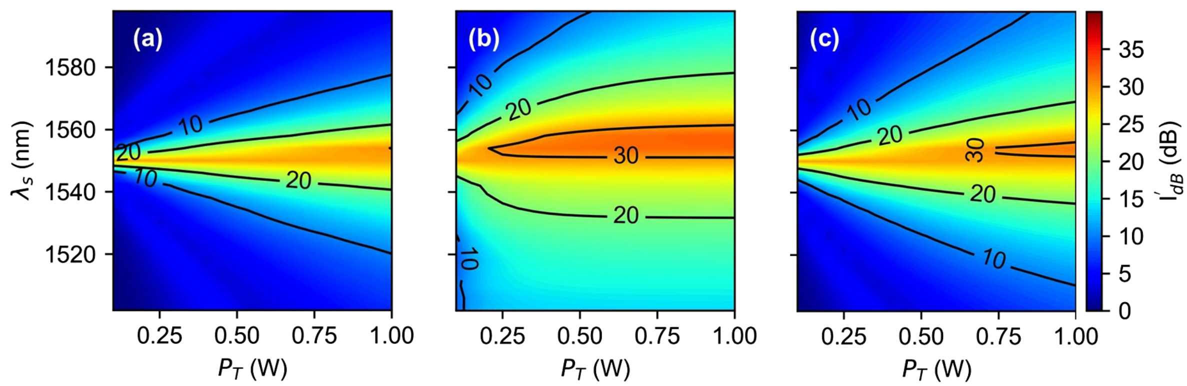

Fig. 9. Overall isolation bandwidth, I'_{dB} as a function of P_T and λ_s after incorporating the mode coupler performance at (a) $\Delta w = -10$ nm, (b) $\Delta w = 0$ nm, and (c) $\Delta w = 10$ nm.

estimate of the experimental g_0 (1×10^3 m^{-1} W^{-1}). The resulting values of I'_{dB} as a function of P_T and λ_s for $w = 560$, 570, and 580 nm are depicted in Figs. 9(a)–9(c). The results illustrate that while the 30 dB isolation line only exists for high P_T, the bandwidths for 10, 20, and 30 dB isolation can increase markedly when switching from low to high P_T, as a consequence of the reduction in L. In addition, at the optimum waveguide width $\Delta w = 0$ and $P_T = 0.5$ W [see Fig. 9(b)], the 10 dB isolation bandwidth exceeds 100 nm while the 30 dB bandwidth is 8 nm (∼1000 GHz).

We can estimate the impact of fabrication uncertainty by incorporating a waveguide width deviation, $\Delta w = \pm 10$ nm into the simulation. As illustrated in Figs. 9(a) and 9(c), the 30 dB isolation line only exists for high P_T, whereas the 10 dB isolation bandwidth at $P_T = 0.5$ W is reduced to 30 nm (∼3700 GHz) and 51 nm (∼6400 GHz) for $\Delta w = -10$ nm and $\Delta w = +10$ nm, respectively.

5. DISCUSSION

In principle, the isolation bandwidth could be improved by inserting a number N of coupler replicas before Port 2. The idea is presented in Fig. 10(a). Such a remedial approach leverages the unique nature of the mode coupler that converts the TE_{21} mode in the wider arm to the TE_{11} mode in the narrower arm [see Figs. 8(b) and 8(d)] while prohibiting the cross coupling of the TE_{11} mode from the wider arm [see Figs. 8(c) and 8(e)], to maximize the I'_{dB} and $|\delta\omega|$ by modifying the term f_{TE21}^{Port2} into $(f_{TE21}^{Port2})^{N+1}$ in Eq. (10). The investigation of isolation improvement due to coupler addition for specific input conditions ($P_T = 0.5$ W and $\Delta w = 0$ nm) is shown in Fig. 10(b). As predicted, the 30 dB isolation bandwidth increases with N and converges to a maximum bandwidth (the black dashed line) at which the term f_{TE21}^{Port2} approaches zero. In our case, an extra coupler ($N = 1$) is sufficient to retrieve the raw isolation [stated in Eq. (8)] from the non-reciprocal mode conversion in the FIBS process. While this approach may be effective, it depends

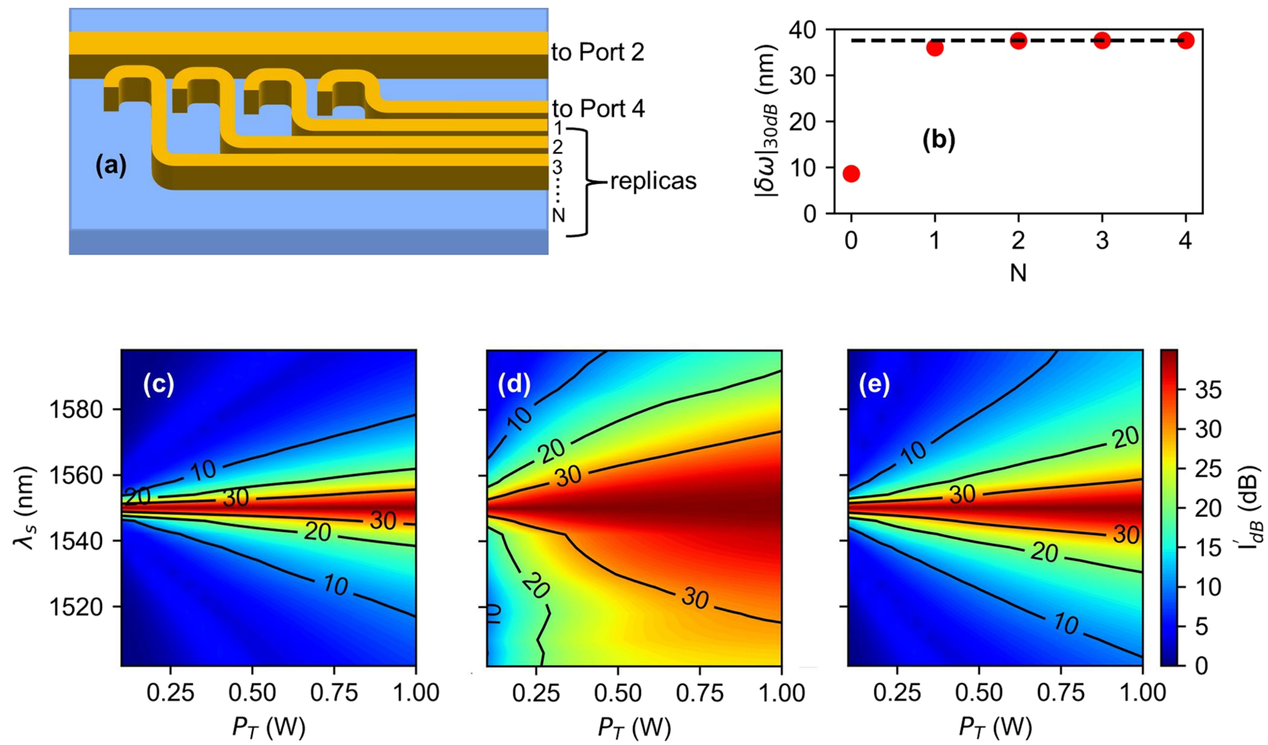

Fig. 10. Improvement of isolation bandwidth: (a) illustration of the placement of the coupler replicas before Port 2, (b) the plot of 30 dB isolation bandwidth, $|\delta\omega|_{30\ \mathrm{dB}}$ versus the number of coupler replicas, N at $P_{\mathrm{total}} = 0.5$ W and $\Delta w = 0$ nm. (c)–(e) The corrected isolation bandwidth, I'_{dB} as a function of P_{T} and λ_s after incorporating an extra mode coupler ($N = 1$) at (c) $\Delta w = -10$ nm, (d) $\Delta w = 0$ nm, and (e) $\Delta w = 10$ nm.

on the efficiency of the mode coupler: using mode couplers with low efficiency would require a large number of coupler replicas, which would significantly increase the device size and overall insertion loss.

The contour plot of the corrected isolation I'_{dB} as a function of P_T and λ_s for $N = 1$ is given in Figs. 10(c)–10(e). At $\Delta w = 0$, the 30 dB isolation bandwidth is increased to 38 nm (∼4700 GHz). It can be seen that, in comparison with Figs. 9(a)–9(c), the isolation bandwidth has been considerably improved in which the 30 dB isolation line now exists for low P_{T} and even with the presence of $\Delta w = \pm 10$ nm. To illustrate, the 10 dB isolation bandwidth has been increased to 34 nm (∼ 4200 GHz) and 59 nm (∼7300 GHz) for $\Delta w = -10$ nm and $\Delta w = +10$ nm, respectively, whereas the 30 dB isolation bandwidths are 5 nm (∼620 GHz) and 10 nm (∼1250 GHz), respectively. These results show that broadband isolation—hundreds of GHz—can be achieved even with the presence of 10 nm structural deviations due to fabrication imperfections.

As a final step in our analysis, we discuss the taper length optimization of the spot size converters and horizontal tapers [see Fig. 2(b)]. If these tapers are too short, the abrupt changes in waveguide width can lead to unwanted mode coupling. There are several widths involved in the whole isolator design that must be accommodated: 570 nm in FIBS waveguide, 562 nm and 1185 nm in the mode coupler, and 1900 nm at the waveguide facet for fiber-to-chip coupling. The biggest change of width occurs between Port 3 (or 4) and the narrow arm of the mode coupler [as shown in Fig. 2(b)] where a width expansion from 570 nm to 1900 nm is required. Concerning the width change of 1300 nm, a taper length scan is performed using Lumerical 3D FDTD. It was found that a taper length of 10 µm is safe (>99.9% transmission) for TE_{11} mode propagation whereas TE_{21} mode will require a taper length of at least 100 µm to suppress any mode coupling (see Section 8 of Supplement 1).

It is also worth commenting on the practical viability of the platform proposed in this work. We numerically demonstrate that the narrow (∼600 nm wide) selenide (As_2Se_3) waveguides have a strong potential for achieving high Brillouin gains ($g_0 \approx 2.4 \times 10^4$ m^{-1} W^{-1} using the phonon viscosity coefficients estimated from 13.2 MHz Brillouin linewidth in Abedin work [54]). From the literature, the As_2Se_3 family (GeAsSe [72] or Ag−As_2Se_3 [73]) possesses a higher intrinsic material absorption at 1550 nm than As_2S_3 [74]. In addition, the waveguide sidewall roughness inherited from the dry-etching can also lead to large propagation loss and mode coupling, in particular for the higher-order optical modes. The propagation loss can range from sub dB/cm to a few dB/cm depending on the etching recipe and waveguide geometry [74]. Such losses are identical in both propagation directions and the overall isolation will not be affected when $\Delta q_{pm} = 0$. However, they can lead to a shorter effective length, from which a higher pump power will be required to maintain such a large device operational bandwidth provided the damage threshold of the waveguide is not exceeded. Therefore, engineering the waveguide loss should be carried out in the future to improve energy efficiency of the proposed Brillouin isolators.

6. CONCLUSION

To summarize, we have carried out an extensive study on an SBS-based optical isolator from both dimensional optimization and fabrication error perspectives. We have shown that the acoustic confinement from the FIBS process can be improved by engineering the waveguide dimension and utilizing an appropriate optical mode transition. More interestingly, the polarization of the acoustic displacement field relies on the choice of the spatial optical mode pairs. Through waveguide dispersion tailoring, a 30 dB isolation bandwidth of 38 nm (∼4700 GHz) can be achieved in a 570 nm × 700 nm As_2Se_3 waveguide with a pump power of 500 mW while the bandwidth is reduced to 5–10 nm at a width error of ±10 nm. Together with fabrication-tolerant mode couplers and the coupler insertion scheme proposed, we have shown that the overall isolation achieved can be solely dependent on the raw isolation from the FIBS process. The simulation and modeling efforts in this work take us one step closer to realizing the on-chip Brillouin-based optical isolator.

3 **Funding.** Australian Research Council (DP200101893).

Disclosures. The authors declare no conflicts of interest.

Data availability. Data underlying the results presented in this paper are not publicly available at this time but may be obtained from the authors upon
4 reasonable request.

Supplemental document. See Supplement 1 for supporting content.

REFERENCES

5
1. D. Jalas, A. Petrov, M. Eich, W. Freude, S. Fan, Z. Yu, R. Baets, M. Popović, A. Melloni, J. D. Joannopoulos, M. Vanwolleghem, C. R. Doerr, and H. Renner, “What is-and what is not-an optical isolator,” Nat. Photonics **7**, 579–582 (2013).
2. L. J. Aplet and J. W. Carson, “A Faraday effect optical isolator,” Appl. Opt. **3**, 544–545 (1964).
3. Y. Shoji, T. Mizumoto, H. Yokoi, I. W. Hsieh, and R. M. Osgood, “Magneto-optical isolator with silicon waveguides fabricated by direct bonding,” Appl. Phys. Lett. **92**, 071117 (2008).
4. M.-C. Tien, T. Mizumoto, P. Pintus, H. Kromer, and J. E. Bowers, “Silicon ring isolators with bonded nonreciprocal magneto-optic garnets,” Opt. Express **19**, 11740–11745 (2011).
5. Y. Sobu, Y. Shoji, K. Sakurai, and T. Mizumoto, “GaInAsP/InP MZI waveguide optical isolator integrated with spot size converter,” Opt. Express **21**, 15373–15381 (2013).
6. D. Huang, P. Pintus, C. Zhang, Y. Shoji, T. Mizumoto, and J. E. Bowers, “Electrically driven and thermally tunable integrated optical isolators for silicon photonics,” IEEE J. Sel. Top. Quantum Electron. **22**, 271–278 (2016).
7. D. L. Sounas and A. Alù, “Non-reciprocal photonics based on time modulation,” Nat. Photonics **11**, 774–783 (2017).
8. L. Bi, J. Hu, P. Jiang, D. H. Kim, G. F. Dionne, L. C. Kimerling, and C. A. Ross, “On-chip optical isolation in monolithically integrated non-reciprocal optical resonators,” Nat. Photonics **5**, 758–762 (2011).
9. Q. Du, C. Wang, Y. Zhang, Y. Zhang, T. Fakhrul, W. Zhang, C. Gonçalves, C. Blanco, K. Richardson, L. Deng, C. A. Ross, L. Bi, and J. Hu, “Monolithic on-chip magneto-optical isolator with 3 dB insertion loss and 40 dB isolation ratio,” ACS Photonics **5**, 5010–5016 (2018).
10. K. Gallo, G. Assanto, K. R. Parameswaran, and M. M. Fejer, “All-optical diode in a periodically poled lithium niobate waveguide,” Appl. Phys. Lett. **79**, 314 (2001).
11. L. Fan, L. T. Varghese, J. Wang, Y. Xuan, A. M. Weiner, and M. Qi, “Silicon optical diode with 40 dB nonreciprocal transmission,” Opt. Lett. **38**, 1259–1261 (2013).
12. F. Nazari, N. Bender, H. Ramezani, M. K. Moravvej-Farshi, D. N. Christodoulides, and T. Kottos, “Optical isolation via PT-Symmetric nonlinear Fano resonances,” Opt. Express **22**, 9574–9584 (2014).
13. N. Bender, S. Factor, J. D. Bodyfelt, H. Ramezani, D. N. Christodoulides, F. M. Ellis, and T. Kottos, “Observation of asymmetric transport in structures with active nonlinearities,” Phys. Rev. Lett. **110**, 234101 (2013).
14. A. E. Miroshnichenko, E. Brasselet, and Y. S. Kivshar, “Reversible optical nonreciprocity in periodic structures with liquid crystals,” Appl. Phys. Lett. **96**, 063302 (2010).
15. J. Wang, L. Fan, L. T. Varghese, H. Shen, Y. Xuan, B. Niu, and M. Qi, “A theoretical model for an optical diode built with nonlinear silicon microrings,” J. Lightwave Technol. **31**, 313–323 (2013).
16. L. Chang, X. Jiang, S. Hua, C. Yang, J. Wen, L. Jiang, G. Li, G. Wang, and M. Xiao, “Parity-time symmetry and variable optical isolation in active-passive- coupled microresonators,” Nat. Photonics **8**, 524–529 (2014).
17. L. Fan, J. Wang, L. T. Varghese, H. Shen, B. Niu, Y. Xuan, A. M. Weiner, and M. Qi, “An all-silicon passive optical diode,” Science **335**, 447–450 (2012).
18. B. Peng, S. K. Özdemir, F. Lei, F. Monifi, M. Gianfreda, G. L. Long, S. Fan, F. Nori, C. M. Bender, and L. Yang, “Parity–time-symmetric whispering-gallery microcavities,” Nat. Phys. **10**, 394–398 (2014).
19. Y. Shi, Z. Yu, and S. Fan, “Limitations of nonlinear optical isolators due to dynamic reciprocity,” Nat. Photonics **9**, 388–392 (2015).
20. M. S. Kang, A. Butsch, and P. St.J. Russell, “Reconfigurable light-driven opto-acoustic isolators in photonic crystal fibre,” Nat. Photonics **5**, 549–553 (2011).
21. X. Huang and S. Fan, “Complete all-optical silica fiber isolator via stimulated Brillouin scattering,” J. Lightwave Technol. **29**, 2267–2275 (2011).
22. H. Lira, Z. Yu, S. Fan, and M. Lipson, “Electrically driven nonreciprocity induced by interband photonic transition on a silicon chip,” Phys. Rev. Lett. **109**, 033901 (2012).
23. C. G. Poulton, R. Pant, A. Byrnes, S. Fan, M. J. Steel, and B. J. Eggleton, “Design for broadband on-chip isolator using stimulated Brillouin scattering in dispersion-engineered chalcogenide waveguides,” Opt. Express **20**, 21235–21246 (2012).
24. L. D. Tzuang, K. Fang, P. Nussenzveig, S. Fan, and M. Lipson, “Non-reciprocal phase shift induced by an effective magnetic flux for light,” Nat. Photonics **8**, 701–705 (2014).
25. C. H. Dong, Z. Shen, C. L. Zou, Y. L. Zhang, W. Fu, and G. C. Guo, “Brillouin-scattering-induced transparency and non-reciprocal light storage,” Nat. Commun. **6**, 6193 (2015).
26. Z. Shen, Y. L. Zhang, Y. Chen, C. L. Zou, Y. F. Xiao, X. B. Zou, F. W. Sun, G. C. Guo, and C. H. Dong, “Experimental realization of optomechanically induced non-reciprocity,” Nat. Photonics **10**, 657–661 (2016).
27. F. Ruesink, M. A. Miri, A. Alù, and E. Verhagen, “Nonreciprocity and magnetic-free isolation based on optomechanical interactions,” Nat. Commun. **7**, 13662 (2016).
28. J. H. Kim, S. Kim, and G. Bahl, “Complete linear optical isolation at the microscale with ultralow loss,” Sci. Rep. **7**, 1–9 (2017).
29. K. Fang, J. Luo, A. Metelmann, M. H. Matheny, F. Marquardt, A. A. Clerk, and O. Painter, “Generalized non-reciprocity in an optomechanical circuit via synthetic magnetism and reservoir engineering,” Nat. Phys. **13**, 465–471 (2017).
30. D. B. Sohn, S. Kim, and G. Bahl, “Time-reversal symmetry breaking with acoustic pumping of nanophotonic circuits,” Nat. Photonics **12**, 91–97 (2018).
31. Z. Shen, Y. L. Zhang, Y. Chen, F. W. Sun, X. B. Zou, G. C. Guo, C. L. Zou, and C. H. Dong, “Reconfigurable optomechanical circulator and directional amplifier,” Nat. Commun. **9**, 1–6 (2018).
32. F. Ruesink, J. P. Mathew, M. A. Miri, A. Alù, and E. Verhagen, “Optical circulation in a multimode optomechanical resonator,” Nat. Commun. **9**, 1798 (2018).
33. E. A. Kittlaus, N. T. Otterstrom, P. Kharel, S. Gertler, and P. T. Rakich, “Non-reciprocal interband Brillouin modulation,” Nat. Photonics **12**, 613–619 (2018).

34. E. A. Kittlaus, W. M. Jones, P. T. Rakich, N. T. Otterstrom, R. E. Muller, and M. Rais-Zadeh, "Electrically driven acousto-optics and broadband non-reciprocity in silicon photonics," Nat. Photonics **15**, 43–52 (2021).
35. D. B. Sohn, O. E. Örsel, and G. Bahl, "Electrically driven optical isolation through phonon-mediated photonic Autler–Townes splitting," Nat. Photonics **15**, 822–827 (2021).
36. H. Tian, J. Liu, A. Siddharth, R. N. Wang, T. Blésin, J. He, T. J. Kippenberg, and S. A. Bhave, "Magnetic-free silicon nitride integrated optical isolator," Nat. Photonics **15**, 828–836 (2021).
37. M. Merklein, B. Stiller, K. Vu, P. Ma, S. J. Madden, and B. J. Eggleton, "On-chip broadband nonreciprocal light storage," Nanophotonics **10**, 75–82 (2021).
38. B. J. Eggleton, B. Luther-Davies, and K. Richardson, "Chalcogenide photonics," Nat. Photonics **5**, 141–148 (2011).
39. R. Pant, C. Poulton, H. MacFarlane, L. Thevenaz, D. Y. Choi, J. Steve, S. J. Madden, B. Luther-Davies, and B. J. Eggleton, "On-chip stimulated Brillouin scattering," in *Optics InfoBase Conference Papers* (Pergamon, 2011), Vol. **2**, pp. 19286–19291.
40. T. F. S. Büttner, M. Merklein, I. V. Kabakova, D. D. Hudson, D.-Y. Choi, B. Luther-Davies, S. J. Madden, and B. J. Eggleton, "Phase-locked, chip-based, cascaded stimulated Brillouin scattering," Optica **1**, 311–314 (2014).
41. B. Morrison, D. Marpaung, R. Pant, E. Li, D. Y. Choi, S. Madden, B. Luther-Davies, and B. J. Eggleton, "Tunable microwave photonic notch filter using on-chip stimulated Brillouin scattering," Opt. Commun. **313**, 85–89 (2014).
42. M. Merklein, I. V. Kabakova, T. F. S. Büttner, D. Y. Choi, B. Luther-Davies, S. J. Madden, and B. J. Eggleton, "Enhancing and inhibiting stimulated Brillouin scattering in photonic integrated circuits," Nat. Commun. **6**, 6396 (2015).
43. B. J. Eggleton, C. G. Poulton, P. T. Rakich, M. J. Steel, and G. Bahl, "Brillouin integrated photonics," Nat. Photonics **13**, 664–677 (2019).
44. D. Marpaung, B. Morrison, M. Pagani, R. Pant, D.-Y. Choi, B. Luther-Davies, S. J. Madden, and B. J. Eggleton, "Low-power, chip-based stimulated Brillouin scattering microwave photonic filter with ultrahigh selectivity," Optica **2**, 76–83 (2015).
45. Y. Liu, A. Choudhary, G. Ren, D. Choi, A. Casas-Bedoya, B. Morrison, P. Ma, T. G. Nguyen, A. Mitchell, S. J. Madden, D. Marpaung, and B. J. Eggleton, "Circulator-free Brillouin photonic planar circuit," Laser Photonics Rev. **15**, 2000481 (2021).
46. R. M. Shelby, M. D. Levenson, and P. W. Bayer, "Guided acoustic-wave Brillouin scattering," Phys. Rev. B **31**, 5244–5252 (1985).
47. G. Bashan, H. H. Diamandi, Y. London, K. Sharma, K. Shemer, E. Zehavi, and A. Zadok, "Forward stimulated Brillouin scattering and opto-mechanical non-reciprocity in standard polarization maintaining fibres," Light Sci. Appl. **10**, 119 (2021).
48. E. A. Kittlaus, H. Shin, and P. T. Rakich, "Large Brillouin amplification in silicon," Nat. Photonics **10**, 463–467 (2016).
49. C. Wolff, P. Gutsche, M. J. Steel, B. J. Eggleton, and C. G. Poulton, "Power limits and a figure of merit for stimulated Brillouin scattering in the presence of third and fifth order loss," Opt. Express **23**, 26628–26638 (2015).
50. C. Wolff, M. J. A. Smith, B. Stiller, and C. G. Poulton, "Brillouin scattering—theory and experiment: tutorial," J. Opt. Soc. Am. B **38**, 1243–1269 (2021).
51. C. Wolff, M. J. Steel, and C. G. Poulton, "Formal selection rules for Brillouin scattering in integrated waveguides and structured fibers," Opt. Express **22**, 32489–32501 (2014).
52. J. Song, X. Guo, W. Peng, J. Pan, L. Wan, T. Feng, S. Zeng, D. Liu, B. Zhang, M. Zhang, and Z. Li, "Stimulated Brillouin scattering in low-loss Ge25Sb10S65 Chalcogenide waveguides," J. Lightwave Technol. **39**, 5048–5053 (2021).
53. B. Auld, *Acoustic Fields and Waves in Solids* (1973).
54. K. S. Abedin, "Observation of strong stimulated Brillouin scattering in single-mode As_2Se_3 chalcogenide fiber," Opt. Express **13**, 10266–10271 (2005).
55. D. K. Biegelsen, "Photoelastic tensor of silicon and the volume dependence of the average gap," Phys. Rev. Lett. **32**, 1196 (1974).
56. M. J. A. Smith, B. T. Kuhlmey, C. M. de Sterke, C. Wolff, M. Lapine, and C. G. Poulton, "Metamaterial control of stimulated Brillouin scattering," Opt. Lett. **41**, 2338–2341 (2016).
57. C. Florea, M. Bashkansky, Z. Dutton, J. Sanghera, P. Pureza, and I. Aggarwal, "Stimulated Brillouin scattering in single-mode As_2S_3 and As_2Se_3 chalcogenide fibers," Opt. Express **14**, 12063–12070 (2006).
58. R. K. Galkiewicz and J. Tauc, "Photoelastic properties of amorphous As_2S_3," Solid State Commun. **10**, 1261–1264 (1972).
59. I. C. M. Littler, L. B. Fu, E. C. Mägi, D. Pudo, and B. J. Eggleton, "Widely tunable, acousto-optic resonances in chalcogenide As_2Se_3 fiber," Opt. Express **14**, 8088–8095 (2006).
60. Y. Ohmachi and N. Uchida, "Vitreous As_2Se_3; investigation of acousto-optical properties and application to infrared modulator," J. Appl. Phys. **43**, 1709–1712 (1972).
61. C. Wolff, M. J. Steel, B. J. Eggleton, and C. G. Poulton, "Stimulated Brillouin scattering in integrated photonic waveguides: forces, scattering mechanisms, and coupled-mode analysis," Phys. Rev. A **92**, 013836 (2015).
62. B. C. P. Sturmberg, K. B. Dossou, M. J. A. Smith, B. Morrison, C. G. Poulton, and M. J. Steel, "Finite element analysis of stimulated Brillouin scattering in integrated photonic waveguides," J. Lightwave Technol. **37**, 3791–3804 (2019).
63. R. Van Laer, B. Kuyken, D. Van Thourhout, and R. Baets, "Interaction between light and highly confined hypersound in a silicon photonic nanowire," Nat. Photonics **9**, 199–203 (2015).
64. O. Florez, P. F. Jarschel, Y. A. V. Espinel, C. M. B. Cordeiro, T. P. Mayer Alegre, G. S. Wiederhecker, and P. Dainese, "Brillouin scattering self-cancellation," Nat. Commun. **7**, 11759 (2016).
65. E. A. Kittlaus, N. T. Otterstrom, and P. T. Rakich, "On-chip inter-modal Brillouin scattering," Nat. Commun. **8**, 15819 (2017).
66. B. Morrison, A. Casas-Bedoya, G. Ren, K. Vu, Y. Liu, A. Zarifi, T. G. Nguyen, D.-Y. Choi, D. Marpaung, S. J. Madden, A. Mitchell, and B. J. Eggleton, "Compact Brillouin devices through hybrid integration on silicon," Optica **4**, 847–852 (2017).
67. C. G. Poulton, R. Pant, and B. J. Eggleton, "Acoustic confinement and stimulated Brillouin scattering in integrated optical waveguides," J. Opt. Soc. Am. B **30**, 2657–2664 (2013).
68. Z. Zhang, Y. Yu, and S. Fu, "Broadband on-chip mode-division multiplexer based on adiabatic couplers and symmetric Y-junction," IEEE Photonics J. **9**, 6600406 (2017).
69. D. Garcia-Rodriguez, J. L. Corral, and R. Llorente, "Design of asymmetrical directional couplers on ridge and strip SOI technology with high-dimensional variation tolerance," Opt. Lett. **43**, 2491–2494 (2018).
70. D. Dai, J. Wang, and Y. Shi, "Silicon mode (de)multiplexer enabling high capacity photonic networks-on-chip with a single-wavelength-carrier light," Opt. Lett. **38**, 1422–1424 (2013).
71. R. Tang, T. Tanemura, and Y. Nakano, "Integrated reconfigurable unitary optical mode converter using MMI couplers," IEEE Photonics Technol. Lett. **29**, 971–974 (2017).
72. X. Gai, S. Madden, D.-Y. Choi, D. Bulla, and B. Luther-Davies, "Dispersion engineered Ge_115As_24Se_645 nanowires with a nonlinear parameter of 136Wˆ-1mˆ-1 at 1550 nm," Opt. Express **18**, 18866–18874 (2010).
73. D. Y. Choi, X. Gai, S. Madden, R. Wang, and B. Luther-Davies, "Silver-doped arsenic selenide (Ag-As2Se3) waveguides for compact nonlinear optical devices," in *IEEE Photonics Conference, IPC* (2012).
74. X. Gai, T. Han, A. Prasad, S. Madden, D.-Y. Choi, R. Wang, D. Bulla, and B. Luther-Davies, "Progress in optical waveguides fabricated from chalcogenide glasses," Opt. Express **18**, 26635–26646 (2010).